



Structure and electrochemical hydrogen storage characteristics of nanocrystalline and amorphous MgNi-type alloy synthesized by mechanical milling

Yang-huan Zhang^{1,2} · Wei Zhang² · Ze-ming Yuan¹ · Wen-gang Bu² · Yan Qi² · Shi-hai Guo²

Received: 11 July 2019 / Revised: 19 September 2019 / Accepted: 9 October 2019 / Published online: 3 April 2020
© China Iron and Steel Research Institute Group 2020

Abstract

Both element substitution and surface modification were utilized to enhance the electrochemical performances of Mg–Ni-based alloys. Nanocrystalline and amorphous $\text{Mg}_{1-x}\text{Ce}_x\text{Ni}_{0.9}\text{Al}_{0.1}$ ($x=0-0.08$) + 50 wt.% Ni hydrogen storage alloys were synthesized through mechanical milling. The sample alloys show excellent activation property and have good electrochemical hydrogenation and dehydrogenation property at normal temperature. The discharge capacity has a peak value with Ce content varying which is 461.6 mAh/g for 10-h milled alloy, while that of $\text{Ce}_{0.04}$ alloy augments from 352.6 to 536.9 mAh/g with milling time extending from 5 to 30 h. Cycle stability is conspicuously improved with Ce content and milling duration augment. To be specific, when cycle number is fixed at 100, the capacity retention rate augments from 41% to 72% after Ce dosage rising from 0 to 0.08 for the 10-h milled alloy and from 58% to 76% after milling duration extending from 5 to 30 h for $\text{Ce}_{0.06}$ alloy. Additionally, the electrochemical kinetics of the alloys own peak values with Ce proportion varying; however, they always rise with milling duration extending.

Keywords Mg–Ni-based alloy · Ce replacing Mg · Surface modification · Mechanical milling · Electrochemical performance

1 Introduction

Consuming fossil fuels excessively results in a variety of environmental concerns, such as severe air pollution and the greenhouse effect, which have attracted worldwide attention [1]. The widely used Ni–MH batteries in electric vehicles (EV) and hybrid electric vehicles (HEV) are viewed with great promise for reducing fossil fuel consumption and carbon dioxide emission due to their zero emission of greenhouse gases and their abundant fuel sources of hydrogen and oxygen [2]. As a matter of fact, “the regulation of access of new energy automobile production enterprises and products” legislated by the Ministry of Industry and Information

Technology of China in 2009 declared that Ni–MH battery-assisted HEV was defined as a national generalized product, which creates a good developing chance for Ni–MH batteries. However, innovation must be carried out to reduce the cost of a Ni–MH battery system and ameliorate its performance for the purpose of gaining consumer acceptance for EV and HEV.

Miscellaneous metal hydrides have been studied extensively to seek for appropriate hydrogen storage systems. Numerous metal hydrides with potential application prospects have been found. Thereinto, Mg-based hydrogen storage alloys are one kind of candidate with great promise and have received high concerns in the past decades on account of their fairly high discharge capacity and cut-rate materials [3–9]. The research and application of Mg-based hydrogen storage alloys are still the focus of most thesis published by International Symposium on Metal Hydrogen System Fundamental and Applications held in 2016. Many components like $\text{Mg}_{93}\text{Cu}_{7-x}\text{Y}_x$ ($x = 0.67, 1.33$ and 2.00) [10], $\text{Mg}_{2-x}\text{Al}_x\text{Ni}$ ($x = 0, 0.1$) [11, 12] and Mg-6Ni-3Cu (at.%) [13] were successfully designed, and the corresponding samples were fabricated by various methods among which the

✉ Yang-huan Zhang
zhangyh59@sina.com

¹ Key Laboratory of Integrated Exploitation of Baiyun Obo Multi-Metal Resources, Inner Mongolia University of Science and Technology, Baotou 014010, Inner Mongolia, China

² Department of Functional Material Research, Central Iron and Steel Research Institute, Beijing 100081, China

in situ formation and in situ analysis were of great importance [14]. Moreover, different kinds of investigations on Mg-based alloys have been conducted, including the summaries of models that express the process of reaction [15], the complex phase diagrams of multicomponent alloys and the catalytic effects of many kinds of other materials [16]. Nevertheless, the attempt to apply the Mg-based alloys is frustrated by their low discharging capacity at normal temperature and bad electrochemical cycle stability [17–19]. It is a big scientific difficulty to drastically improve the electrochemical property of Mg-based alloys.

It has been found that the formation and growing of a $\text{Mg}(\text{OH})_2$ film on sample particle surface bring up capacity degradation of Mg-based alloys [20]. This film will hinder the charge transferring and hydrogen diffusing reactivities. Furthermore, such detrimental situations will be aggravated by the pulverization of alloys upon cycles, which will form a new active film and generate extra $\text{Mg}(\text{OH})_2$ when touching the electrolyte [21]. The useful ways to prohibit the capacity damping of Mg-based alloy include improving the oxidation resistance of alloys in KOH electrolyte by partially replacing Mg and/or Ni and enhancing anti-pulverization ability of the electrode by lessening the alloy dilatation coefficient during hydriding. Dong et al. [22] replaced part Mg by La and investigated the relationship between the electrochemical property of $\text{La}_{0.80}\text{Mg}_{0.20}\text{Ni}_x$ ($x=3.5\text{--}5.0$) alloys and the ratio $\text{Ni}/(\text{La} + \text{Mg})$. When the ratio is 4.0, the alloy capacity attenuates at the lowest rate. Balcerzak et al. [23] investigated the electrochemical property of $(\text{La}, \text{Mg})_2\text{Ni}_7$ alloys by adjusting La/Mg ratio. They found that the best cycle stability belongs to LaMgNi_7 alloy. Dong et al. [24] partly substituted Ni by $\text{Co}_{0.5}\text{Al}_{0.5}$ in an AB_3 -type hydrogen storage electrode alloy, through which capacity retention ratio of the alloy after 60 charge/discharge cycles increases from 61.2% to 78.7% and its electrochemical kinetic property increases as well.

For enhancing the electrochemical property of Mg-based alloys, mechanical coating as one of the surface modification methods has proved to be a valid approach. Wang et al. [25] ball-milled MmMg_{12} alloy with Ni powders and found that the initial discharge capacity grows from 964 to 1164 mAh/g as the percentage of Ni raises from 150 to 200 wt.%. Santos et al. [26] researched the impact of mechanical coating on a Mg-50 at.% Ni alloy with Ni and Ni-5 at.% Al, which exhibits a significant enhancement of the maximal discharge capacity and cycle stability. Sun et al. [27] improved $\text{Mg}_{24}\text{Ni}_{10}\text{Cu}_2$ alloy in discharge capacity and electrochemical kinetics by mechanical milling with Ni powder.

Our previous studies show that adding Ce can improve the electrochemical property of AB_2 -type and REMg_{12} -type alloys [28, 29]. Meanwhile, Young et al. [30] reported that the corrosion resistance of alloys in KOH electrolyte can be enhanced obviously along with Al content raise.

Besides the improvement in corrosion resistance of alloys, Ni coating layer also acts as a key electrocatalyst in the polarization course, for instance, accelerating hydrogen diffusion and charge transfer on the surface of samples [31, 32]. In this work, Mg and Ni of Mg–Ni-based alloys were partially replaced by Ce and Al separately in order to obtain many-sided better electrochemical performances. Mechanically coated Ni powder was used for surface modification. We investigated the impacts on the properties of $\text{Mg}_{1-x}\text{Ce}_x\text{Ni}_{0.9}\text{Al}_{0.1}$ ($x=0\text{--}0.08$) + 50 wt.% Ni (50 wt.% Ni is represented by 50Ni) alloys in the aspect of electrochemistry made by changing milling duration and Ce proportion and discussed the mechanism.

2 Experimental

A vacuum induction furnace was used to prepare $\text{Mg}_{1-x}\text{Ce}_x\text{Ni}_{0.9}\text{Al}_{0.1}$ ($x=0, 0.02, 0.04, 0.06, 0.08$) alloys. All of the raw materials with 99.99% purity were obtained from CISRI. For restraining the volatilizing loss of Mg, the process was executed under the helium atmosphere of 0.04 MPa. Subsequently, the molten alloy was infused in a water-cooled copper-formed mold to get the cast ingots. A portion of these obtained alloys was processed into approximately 50- μm -sized powders. The sample particle is mixed with nickel particle in a mass ratio of 2:1; after that, rustless steel balls are mixed with the mixed powders in a mass ratio of 35:1 in mill pots. Then, a planetary miller was used to grind the powders under argon atmosphere for protecting these powders from oxidization. The rotational velocity of the planetary miller was 135 r/min and the durations were 5, 10, 20 and 30 h, respectively. The samples were symbolized by Ce_0 , $\text{Ce}_{0.02}$, $\text{Ce}_{0.04}$, $\text{Ce}_{0.06}$, and $\text{Ce}_{0.08}$ for description according to Ce component.

X-ray diffraction (XRD, D/max/2400) with the testing parameters of 10 ($^\circ$)/min, 40 kV and 160 mA executed by Cu $\text{K}\alpha 1$ radiation percolated with plumbago was utilized to measure phase structure. A Philips scanning electron microscope (SEM, QUANTA 400) was used to observe the morphologies of as-cast alloys. The energy-dispersive X-ray detector (EDX) was used to measure the as-milled $\text{Mg}_{1-x}\text{Ce}_x\text{Ni}_{0.9}\text{Al}_{0.1}$ ($x=0\text{--}0.08$) + 50Ni alloys. In order to measure the particle size of samples after ball milling, a dry laser particle size analyzer (HELOS-RODOS) produced by Sympatec GmbH was utilized. The observation of particle of these alloys was processed with the help of a high-resolution transmission electron microscope (HRTEM, JEM-2100F). The crystalline state was observed by electron diffraction (ED).

The admixture of alloy and nickel carbonyl particles with 1:4 in the mass ratio was chill molded under 35 MPa into circular pole slice whose diameter and mass were 15 mm and

1 g, respectively. A tri-pole open cell was used to test electrochemical property at 303 K, containing a working pole (metal hydride pole), an agglomerative Ni(OH)₂/NiOOH negative pole and a contrast electrode of Hg/HgO, soaked in 6 mol/L KOH solution. The voltage between the negative and contrast electrodes was recognized as the discharging voltage. For each circulation, the pole was firstly recharged at a constant current density, and then, after a 15-min rest, it began to discharge at the same current density till -500 mV.

The measurement of electrochemical impedance spectra (EIS) and potentiodynamic polarization curves of samples was taken by a battery testing system (PARSTAT 2273) at 303 K. Ahead of measuring, the poles were charged and discharged for activation. These new poles were entirely charged firstly and subsequently kept static for 2 h till the stabilization of open-circuit potential. At the half depth of discharge, the measurement of EIS was taken with frequency ranging from 10 kHz to 5 mHz at 5 mV alternating current amplitude. At 5 mV/s scanning velocity and potential range of -1.2 to +1.0 V, the potentiodynamic polarization curves were tested. As to the constant voltage discharging process, the entirely charged electrode was discharged at 500 mV for 5000 s on a battery testing system (PARSTAT 2273).

3 Results and discussion

3.1 Microstructure characterization

Figure 1 presents XRD curves of the as-milled samples of Mg_{1-x}Ce_xNi_{0.9}Al_{0.1} (x = 0–0.08) + 50Ni alloy. It can be identified with the International Centre for Diffraction Data (ICDD) that the as-milled alloys have polyphase structures including a principal phase Mg₂Ni and minor phases of Ni, AlNi and MgNi₂. A new phase Ce₂Ni₇ appears, but MgNi₂ disappears after the substitution of Ce for Mg. The quantity of Ce₂Ni₇ phase distinctly goes up in the wake of Ce increasing. When Ce content reaches 0.04, AlNi phase can hardly be seen. The sharp diffraction peaks demonstrate the crystal structure of the as-milled (10 h) alloys, as shown in Fig. 1a. The major diffraction peaks around 45° of Mg₂Ni and Ni phases are overlapping and indistinguishable. Figure 1b shows that with milling time increasing, the nanocrystallization and/or amorphization appears reflected by the considerably widened peaks of Mg₂Ni and Ce₂Ni₇, while the sharp peaks of Ni manifest Ni remaining crystalline. In general, the change in crystallite dimension and nonhomogeneous strain will lead to diffraction peaks broadening. The inner stress augments in the wake of prolonging milling duration, and then, the more defects will be generated in the samples.

Figure 2 exhibits SEM photographs belonging to the as-cast Mg_{1-x}Ce_xNi_{0.9}Al_{0.1} (x = 0–0.08) alloys from which the morphological characteristics can be investigated. Ce substituting Mg brings about an obvious thinning of grains

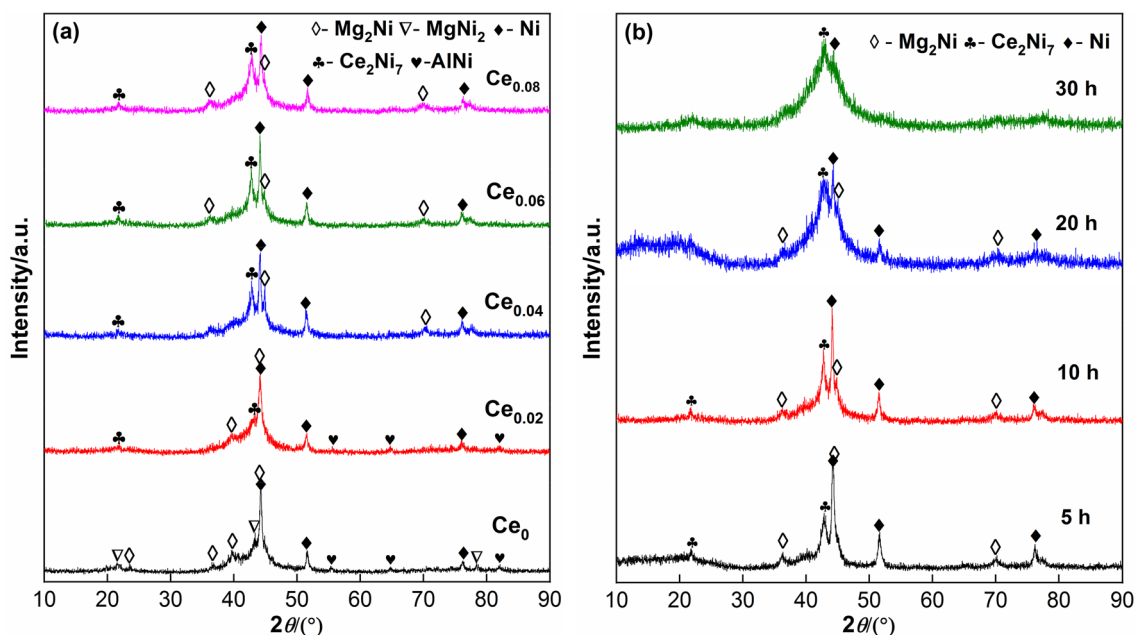


Fig. 1 XRD curves of as-milled Mg_{1-x}Ce_xNi_{0.9}Al_{0.1} (x = 0–0.08) + 50Ni alloys. **a** Milled for 10 h; **b** Ce_{0.06} alloy

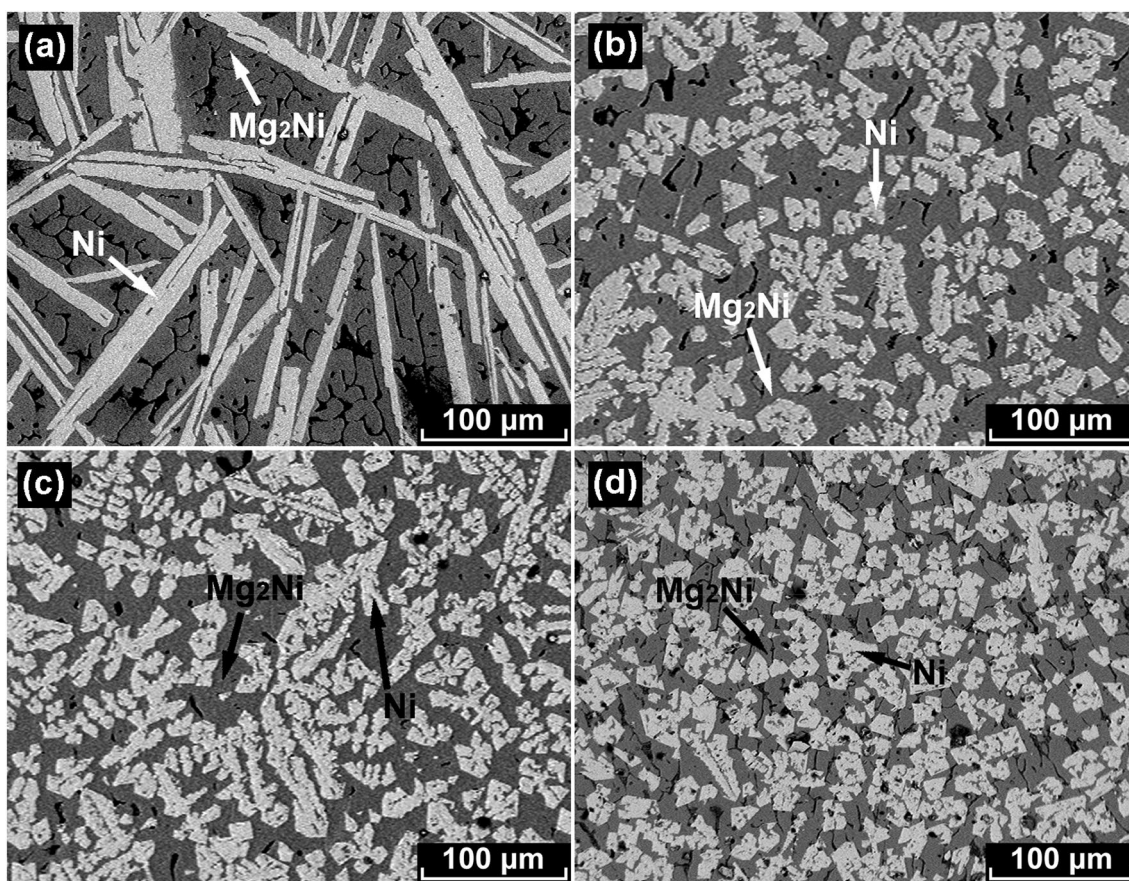


Fig. 2 SEM micrographs of as-cast $\text{Mg}_{1-x}\text{Ce}_x\text{Ni}_{0.9}\text{Al}_{0.1}$ ($x=0-0.08$) alloys. **a** Ce_0 alloy; **b** $\text{Ce}_{0.02}$ alloy; **c** $\text{Ce}_{0.04}$ alloy; **d** $\text{Ce}_{0.08}$ alloy

of the as-cast alloys. A similar result has been found after studying other Mg-based alloys [29, 33]. The strength and toughness of alloys can be improved by refining grain size, thereby enhancing their ability of anti-pulverization [34].

Morphological characteristics and crystal state of samples were observed through HRTEM, as delineated in Fig. 3. The as-milled alloys present amorphous and nanocrystalline structures. The Debye–Scherrer rings grow wider and blurrier as Ce content and grinding time raise, which means that the nanocrystalline size shrinks and the amorphous phase increases. This is because of a large amount of inner energy stored during the grinding process, which results in the non-stationary state of the lattice and forms extra fine particles or amorphous structures in the end. With ball-milling time prolonging and Ce content increasing, the microscopic structure becomes more disordered and more and more crystal defects appear, including dislocations, stacking faults and crystal boundaries. The increasing lattice defects not only refine the grain size but also contribute lots of channels for hydrogen diffusing inside alloys [35].

The particle size of the as-milled alloys was measured using a particle size analyzer. We take the particle size at 50% cumulative distribution as the average particle size of

the alloy powders in this manuscript. As shown in Fig. 4, the particle size of sample alloys was shrunk with Ce content raise and milling duration extension.

3.2 Electrochemical property

3.2.1 Electrochemical cycle stability

The ability of an electrode restraining capacity degradation is known as cycle stability and represented by capacity retaining rate (S_n) as $S_n = C_n/C_{\max} \times 100\%$. In this formula, C_n and C_{\max} symbolize the n th discharge capacity and the maximal discharge capacity at the current density of 300 mA/g, respectively. Figure 5 delineates the evolutions of S_n of the as-milled samples with cycling number, and we can see clearly that the decay velocity of discharge capacity drastically declines in the wake of increasing Ce content and milling duration. For directly showing the influences of Ce content and milling duration on the cycle stability of alloys, these capacity retention ratios at 100th circulation, viz. S_{100} values, are used as a standard. Therefore, S_{100} ($n=100$) value dependences on Ce content and milling duration can be obtained, as Fig. 6 supplies. S_{100} value of these alloys

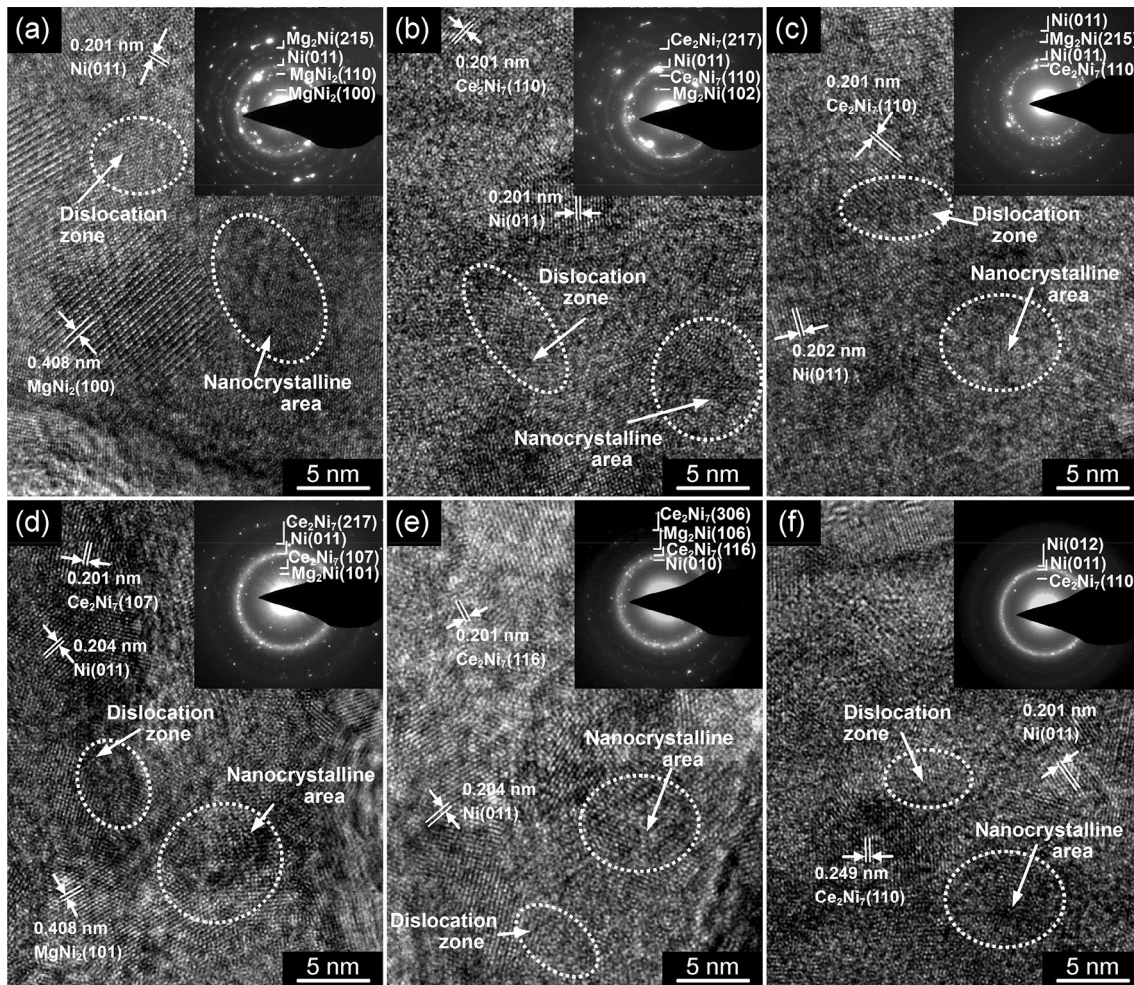


Fig. 3 HRTEM and ED images of as-milled $\text{Mg}_{1-x}\text{Ce}_x\text{Ni}_{0.9}\text{Al}_{0.1}$ ($x=0-0.08$)+50Ni alloys milled for different durations. **a, b, c** Ce_0 , $\text{Ce}_{0.04}$ and $\text{Ce}_{0.08}$ alloys milled for 10 h; **d, e, f** $\text{Ce}_{0.06}$ alloy milled for 10, 20 and 30 h

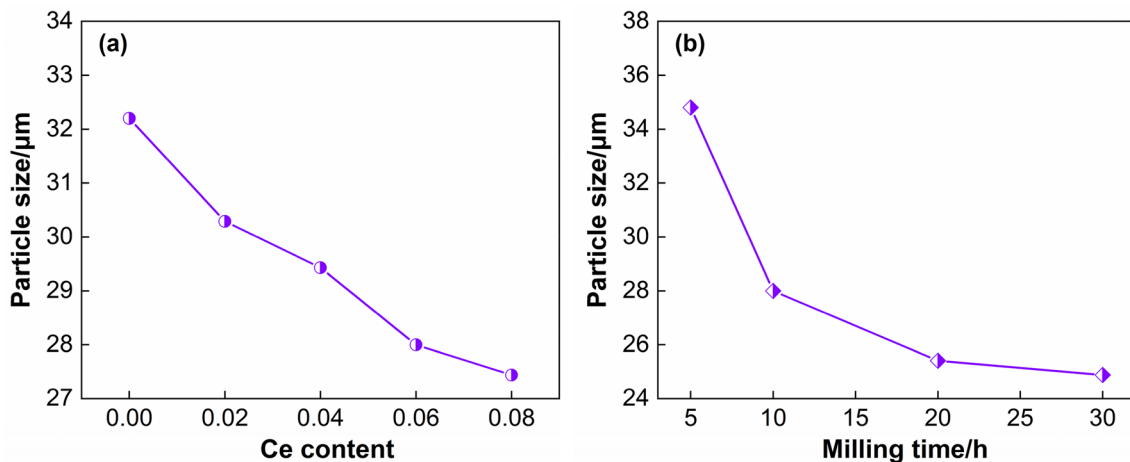


Fig. 4 Evolution of particle size of $\text{Mg}_{1-x}\text{Ce}_x\text{Ni}_{0.9}\text{Al}_{0.1}$ ($x=0-0.08$)+50Ni alloys with Ce content and milling time. **a** Milled for 10 h; **b** $\text{Ce}_{0.06}$ alloy

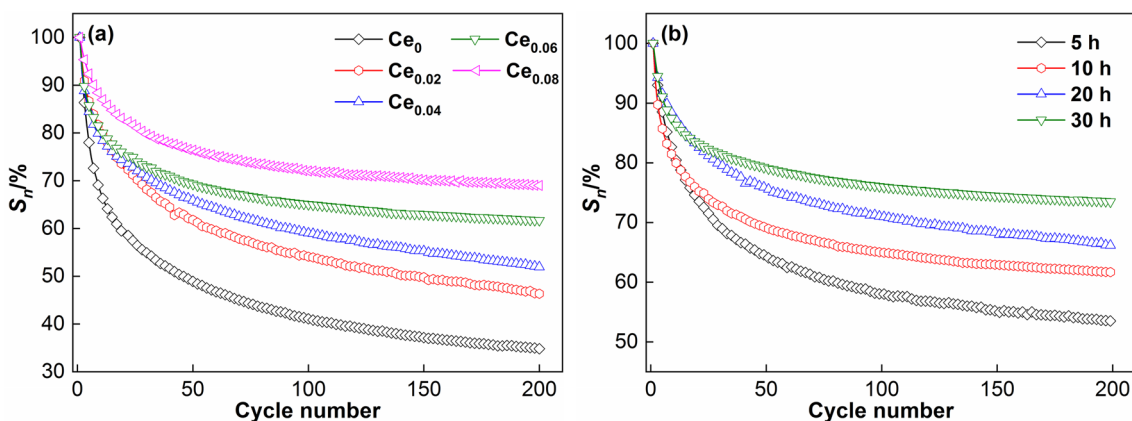


Fig. 5 Evolution of S_n of as-milled $Mg_{1-x}Ce_xNi_{0.9}Al_{0.1}$ ($x=0-0.08$) + 50Ni alloys with cycle number. **a** Milled for 10 h; **b** $Ce_{0.06}$ alloy

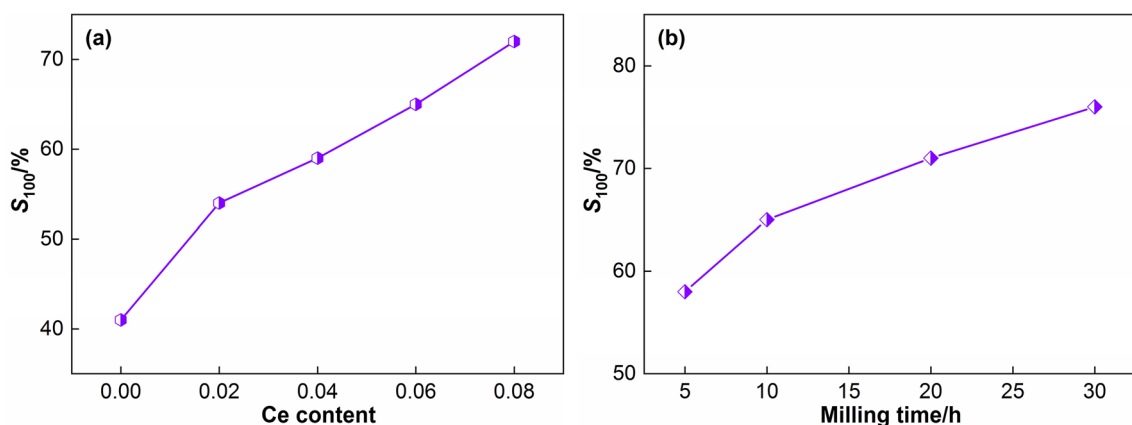


Fig. 6 Evolution of S_{100} of $Mg_{1-x}Ce_xNi_{0.9}Al_{0.1}$ ($x=0-0.08$) + 50Ni alloys with Ce content and milling time. **a** Milled for 10 h; **b** $Ce_{0.06}$ alloy

clearly grows in the wake of increasing Ce content and milling duration. To be specific, increasing Ce content from 0 to 0.08 makes S_{100} value of 10-h milled alloys mount up from 41% to 72%, and S_{100} value of $Ce_{0.06}$ alloy rises from 58% to 76% when prolonging milling duration from 5 to 30 h.

A beneficial influence generates on the cycle stability of Mg-based alloys after Ce replacing Mg partially, which may be related to the enhanced corrosion resistance. Ce will transform to CeO_2 in KOH electrolyte. In aqueous alkali, CeO_2 can be dissolved hardly, so it can be considered as a corrosion-resistant oxide inset amidst the multihole $Mg(OH)_2$ passivation coating. The passivation coating makes the infiltration of OH^- harder and defends internal alloys from being oxidized efficiently. The positive contribution caused by prolonging milling time to cycle stability is highly possibly connected with the appearance of a fine and close Ni cladding layer, as shown in Fig. 7. A mass of Ni can be seen in EDX curve of 30-h milled $Ce_{0.06}$ alloy, which means the formation of a Ni cladding layer during ball-milling process. It is generally known that Ni is provided with high ductility. During

the grinding process, the repeated collision among balls and powders induces mechanical deformations and leads to the alloy powders being covered by a Ni cladding layer. Compared with Fig. 7a, the Ni coating layer in Fig. 7b is more evident. We can deduce that the prolongation of milling time can heighten the compactness of Ni cladding layer, which is beneficial for increasing the cycle stability of alloys. Many other researchers have reported the cycle stability enhancement by forming a core-shell structure as well [36–38].

3.2.2 Activation capability, potential characteristic and discharge capacity

The cycle times demanded for an electrode to achieve its maximum discharging capacity by reduplicative charging and discharging course at an invariable small current density are used to assess its activation capability. The lesser the count of charge-discharge circulation, the better the activation capability will be, and the more suitable for Ni-MH batteries the material will be. Figure 8 exhibits the changes

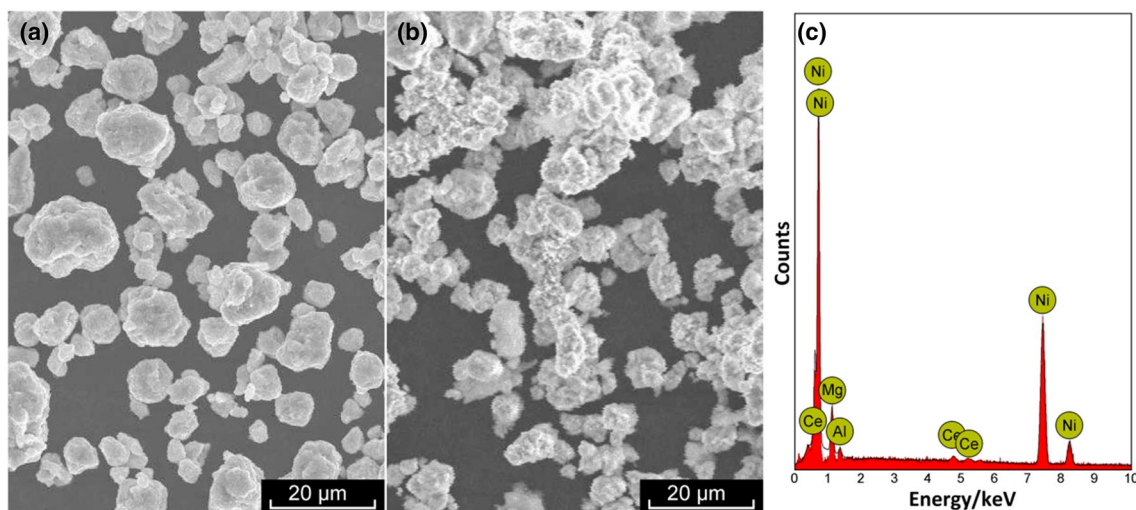


Fig. 7 SEM images (a, b) and EDX curve (c) of as-milled $\text{Ce}_{0.06}$ alloy. **a** Milled for 5 h; **b, c** milled for 30 h

in discharging capacities of the as-milled $\text{Mg}_{1-x}\text{Ce}_x\text{Ni}_{0.9}\text{Al}_{0.1}$ ($x=0-0.08$) + 50Ni alloys with the count of circulations at 60 mA/g. Evidently, the discharge capacities of as-milled alloys can reach their maximum values at the first charge–discharge circulations without any activation, meaning the outstanding activation property of samples. Substituting Mg with Ce has not degenerated the activation property of these samples. This superior activation property is related to the active surface that appeared during ball milling Ni. Besides, the nanocrystalline and ultrafine particles produced through ball milling bring about a large number of interfaces which are instrumental in enhancing the activation capability [39]. Zhao et al. [40] discovered that compared with polycrystalline nickel, the nanocrystalline nickel can absorb hydrogen more tightly as the nanocrystalline nickel surface can accelerate hydrogen dissociation reaction and give rise to an amelioration of activation performance of

the pole. Jafarian et al. [41] found that the electrocatalytic activity for absorbing hydrogen can be enhanced by increasing the surface area of electrodes. Li et al. [42] modified the surface of Mg_2NiH_4 by nano-nickel coating, which improved Mg_2NiH_4 in electrochemical hydrogen storage performance. As we all know, several discharging/charging cycles are needed for the activation of AB_5 -type alloys. Obviously, the activation ability of experimental sample alloys is above that of AB_5 -type alloys.

The discharging potential curves of a battery can characterize its power outputting stability. Longer and more horizontal discharging potential plateaus mean the battery having a more excellent discharging potential characteristic. Figure 9 depicts the discharging potential figures of as-milled $\text{Mg}_{1-x}\text{Ce}_x\text{Ni}_{0.9}\text{Al}_{0.1}$ ($x=0-0.08$) + 50Ni alloys at 60 mA/g. Obviously, the potential plateaus of experimental alloys are slant, which is a common feature

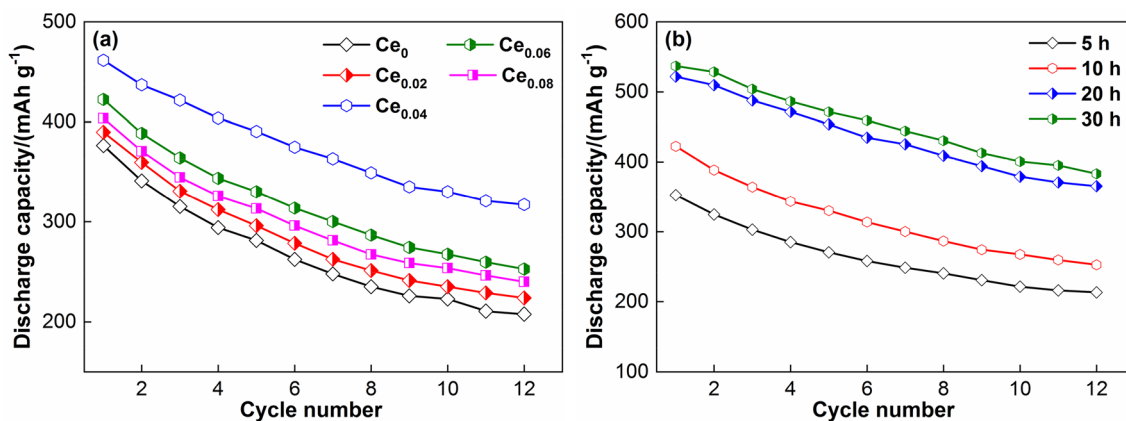


Fig. 8 Evolution of discharge capacity of as-milled $\text{Mg}_{1-x}\text{Ce}_x\text{Ni}_{0.9}\text{Al}_{0.1}$ ($x=0-0.08$) + 50Ni alloys with cycle number. **a** Milled for 10 h; **b** $\text{Ce}_{0.06}$ alloy

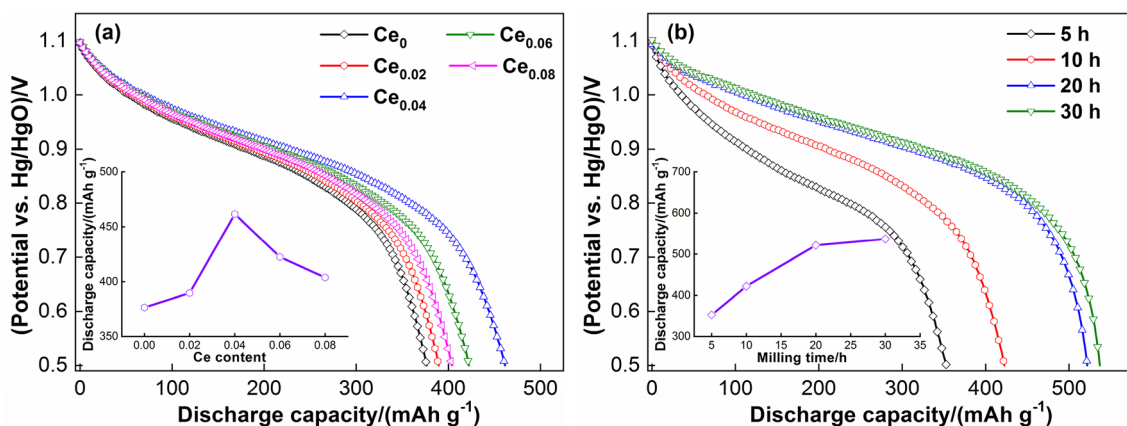


Fig. 9 Discharging potential curves of as-milled $\text{Mg}_{1-x}\text{Ce}_x\text{Ni}_{0.9}\text{Al}_{0.1}$ ($x=0-0.08$) + 50Ni alloys. **a** Milled for 10 h; **b** $\text{Ce}_{0.06}$ alloy

of the potential figures of Mg-based alloys. Very similar results have been reported in many related documents [43, 44]. In addition, it was discovered that raising Ce content and milling duration markedly enhance the discharging potential performance of alloys, including ameliorating discharging potential and extending discharging plateau. The active function of increasing Ce content and milling duration on the potential property is most possibly caused by improving the corrosion resistance and distinctly refining the particles for the fact that crystal boundaries supply convenient channels for hydrogen diffusing [45]. In Sect. 3.3, we will probe the relationship between the hydrogen diffusing rate of alloys with Ce content and milling duration. As is presented in Fig. 9a, b, the discharging capacities of alloys as functions of Ce content and milling duration are described, respectively. The discharge capacity of 10-h milled alloy first ascends and then descends when increasing Ce content, while it always rises for $\text{Ce}_{0.06}$ alloy with milling duration extending. Concretely, the discharging capacity of 10-h milled alloy augments from 376.5 to 461.6 mAh/g firstly and subsequently drops to 403.8 mAh/g when Ce content raises. In the wake of ball-milling duration extending from 5 to 30 h, the discharging capacity of $\text{Ce}_{0.06}$ alloy grows from 352.6 to 536.9 mAh/g. It has been put forward in numerous articles that rare earth substituting Mg makes a beneficial effect on the discharging capacity of Mg-based alloys. Liao et al. [46] replaced Mg by La partly and researched the effect of La/Mg ratio on electrochemical property of La–Mg–Ni alloy. La_2MgNi_9 alloy (La/Mg = 2) has the maximum discharge capacity of 397.5 mAh/g when discharging at 100 mA/g. Yartys and Denys [47] measured the electrochemical property of $\text{RE}_{3-x}\text{Mg}_x\text{Ni}_9$ (RE = La, Pr, Nd and $x=0-2$) alloys whose discharge capacity can reach 400 mAh/g and remains high after 300 charging and discharging cycles.

3.3 Electrochemical kinetics

Electrochemical kinetics property is very important for alloy electrodes and it is usually characterized by high rate discharge ability (HRD) as $\text{HRD} = C_i/C_{60} \times 100\%$, where i represents the current density, and C_i and C_{60} represent the peak values of discharge capacity of the electrodes when charging and discharging at different current densities of i and 60 mA/g severally. Figure 10 delineates the evolutions of HRD values of the as-milled $\text{Mg}_{1-x}\text{Ce}_x\text{Ni}_{0.9}\text{Al}_{0.1}$ ($x=0-0.08$) + 50Ni alloys with current density. HRD distinctly declines in the wake of current density raising. To show the effects of Ce content and milling duration on HRD values more intuitively, we take 300 mA/g as an example. HRD dependences of Ce content and ball-milling duration are able to be derived, as Fig. 10a and b describes severally. HRD initially rises and subsequently declines in the wake of Ce content varying, while it obviously grows with the increase in milling duration. Concretely, HRD ($\text{HRD} = C_{300}/C_{60}$) first goes up from 77.2% (Ce_0 alloy) to 87.6% ($\text{Ce}_{0.02}$ alloy) and then goes down to 79.7% ($\text{Ce}_{0.08}$ alloy) for the as-milled (10 h) alloy, but it augments from 62.7% to 87.5% for $\text{Ce}_{0.06}$ alloy when milling time lengthens from 5 to 30 h.

Generally speaking, the electrochemical HRD principally depends on two factors, viz. the capacity of hydrogen diffusing inside the sample block and the charge shifting velocity on the pole surface [48]. For understanding the kinetics principles of these samples, it is strongly essential to study the influences of Ce content and milling duration on hydrogen diffusing capacity and charge shifting velocity. The hydrogen diffusion coefficient (D) for this kind of sample was assessed with the potential step method according to the report of Volodin et al. [49]. Figure 11 demonstrates the semilogarithmic plots of the current–time response for $\text{Mg}_{1-x}\text{Ce}_x\text{Ni}_{0.9}\text{Al}_{0.1}$ ($x=0-0.08$) + 50Ni alloys at completely

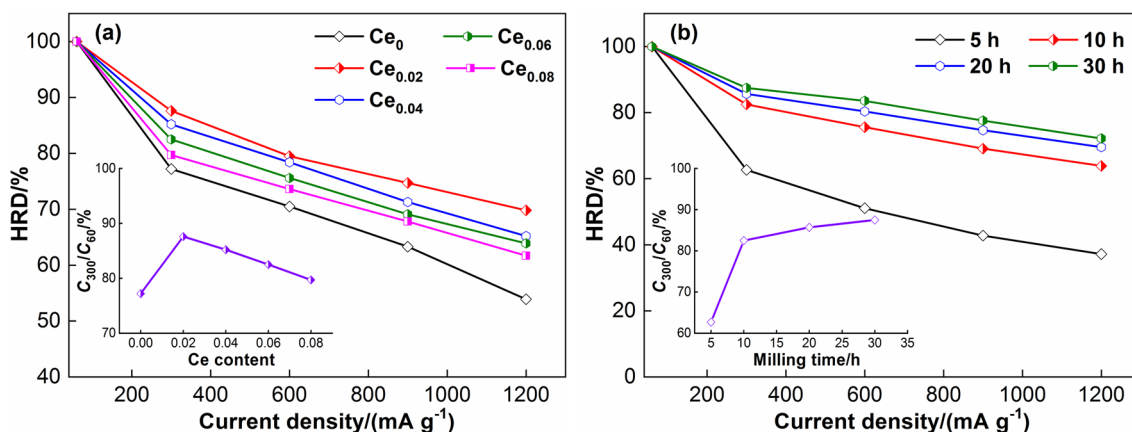


Fig. 10 Evolution of HRD of as-milled $\text{Mg}_{1-x}\text{Ce}_x\text{Ni}_{0.9}\text{Al}_{0.1}$ ($x=0-0.08$) + 50Ni alloys with current density. **a** Milled for 10 h; **b** $\text{Ce}_{0.06}$ alloy

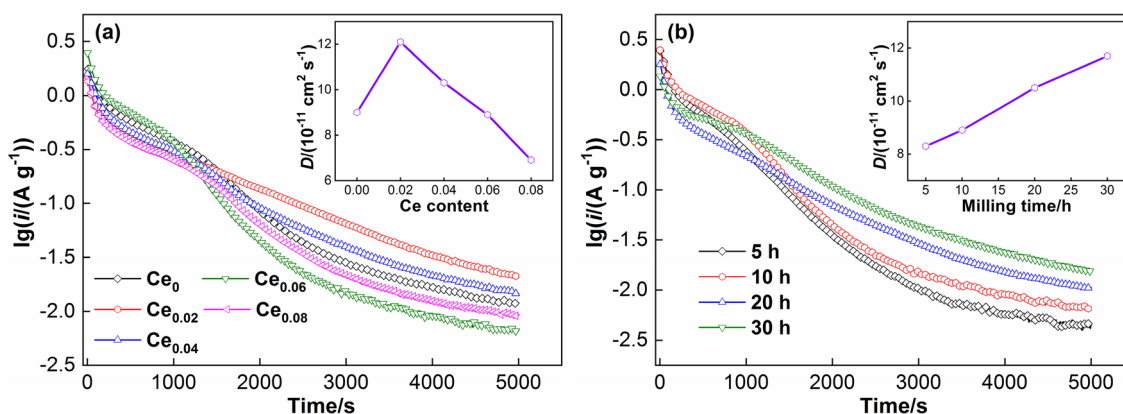


Fig. 11 Semilogarithmic curves of current versus time responses of as-milled $\text{Mg}_{1-x}\text{Ce}_x\text{Ni}_{0.9}\text{Al}_{0.1}$ ($x=0-0.08$) + 50Ni alloys. **a** Milled for 10 h; **b** $\text{Ce}_{0.06}$ alloy

charged status. The value of $\lg i$ drops sharply at first, indicating that the hydrogen concentration above pole surface cuts down on account of the electro-oxidation. Subsequently, the curves become linear by the reason that the velocity controlling process turns from electro-oxidation to hydrogen diffusing inside samples. Through fitting the linear part of the curves, the values of D are able to be figured out depending on Eqs. (1) and (2) as follows [50]:

$$\lg i = \lg \left[\pm \frac{6FD}{a^2} (C_0 - C_s) \right] - \frac{\pi^2 D}{2.303 a^2} t \quad (1)$$

$$D = -\frac{2.303 a^2 d \lg i}{\pi^2 dt} \quad (2)$$

where a is the particle radius, cm; d symbolizes the alloy density, g cm^{-3} ; F stands for the Faraday constant, C mol^{-1} ; C_0 means the initial hydrogen concentration inside the sample, mol cm^{-3} ; C_s is the hydrogen concentration on particle

surface, mol cm^{-3} ; and t represents the discharging time, s. All the alloy powders are approximated as spherical in this experiment. With a particle size analyzer, we got the average particle size which can be treated as the particle diameter. Thus, according to the data in Fig. 4, a value of particle radius can be gotten easily. The values of D obtained from Eq. (2) are inset into Fig. 11a, b severally as functions of Ce content and milling time. D has a peak value in the wake of varying Ce content, while it keeps augmenting with milling duration prolonging.

The potentiodynamic polarization curves of alloys are shown in Fig. 12, through which another significant kinetic parameter of limiting current density is able to be figured out. Every anodic polarization curve has a clear yielding point. The limiting current density is defined as the current value corresponding to the yielding point and symbolized by I_L . The inflection point indicates the appearance of oxidation on pole surface, soon afterward the newly formed oxide coating layer will hinder the permeation of hydrogen atoms

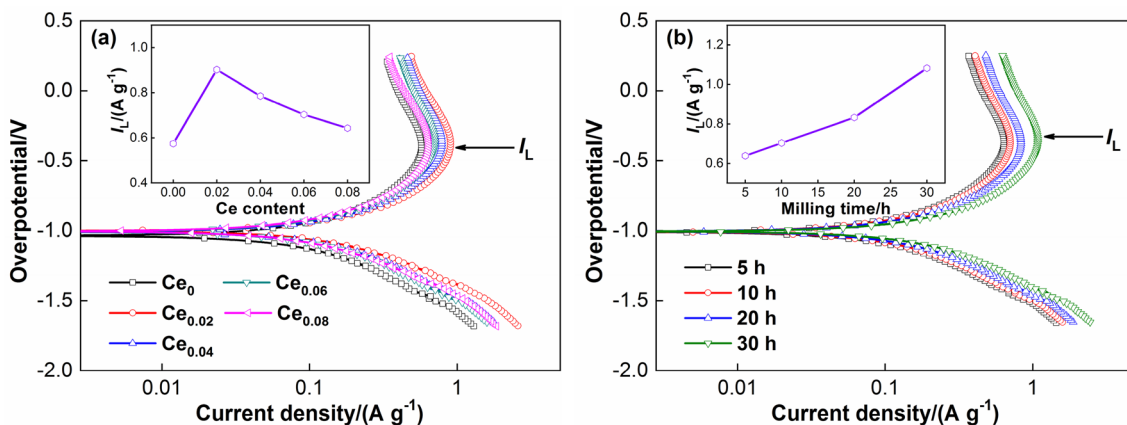


Fig. 12 Potentiodynamic polarization curves of as-milled $Mg_{1-x}Ce_xNi_{0.9}Al_{0.1}$ ($x=0-0.08$) + 50Ni alloys. **a** Milled for 10 h; **b** $Ce_{0.06}$ alloy

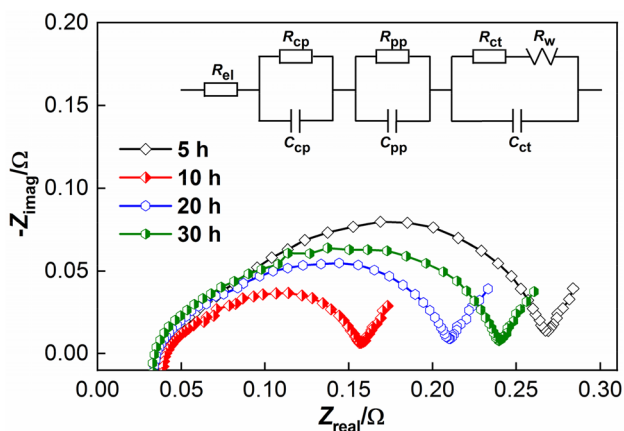


Fig. 13 EIS of $Ce_{0.06}$ alloy milled for different time and equivalent circuit

[51]. Therefore, the value of I_L is viewed as the threshold ampere density for passivating treatment. The dependences of I_L values on Ce content and milling duration are provided in Fig. 12a and b, respectively, based on the potentiodynamic polarization curves. Evidently, I_L value rises primarily and falls subsequently in the wake of Ce content rising, but it always grows up when extending milling duration.

EIS of an alloy sample is usually used to assess the charge transferring velocity on its surface based on Kuriyama’s model [52]. We take the as-milled $Ce_{0.06}$ alloy as a representative and show its EIS curves in Fig. 13. Z_{real} in abscissa means the real part impedance, and Z_{imag} in ordinate represents the imaginary impedance. As is exhibited in Fig. 13, the high- and middle-frequency regions have one distorted capacitive loop and the low-frequency region has linear plots. EIS curves of an alloy pole reflect its electrochemistry process. The minor hemicycle part symbolizes the contact impedance among samples and conducting materials, the

bigger hemicycle part reflects the charge transfer impedance (R_{ct}) on sample surface and the linear part represents Warburg resistance. Figure 13 also presents the equivalent circuit diagram, from which R_{ct} values are able to be received by using the fitting program Z-View. In this equivalent circuit, R_{el} stands for the resistance of the electrolyte between the working and reference electrodes; R_{cp} and C_{cp} represent the contact resistance and capacitance between the current collector and electrode plate, respectively; R_{pp} and C_{pp} symbolize the contact resistance and capacitance between alloy particles, respectively; C_{ct} stands for the charge transfer reaction capacitance on alloy particle surface; and R_w symbolizes Warburg impedance. Both the reaction area and reactivity on sample surface are the key elements for determining the value of R_{ct} [52]. The electrochemical reaction on the sample surface basically depends on apparent activation enthalpy change ($\Delta_r H^*$) which is allowed to be figured out with the formula below [53]:

$$\ln \left(\frac{T}{R_{ct}} \right) = C - \frac{\Delta_r H^*}{RT} \tag{3}$$

where R stands for the gas constant; C means a constant including the surface area; and T represents the specimen temperature, K. For calculating the values of $\Delta_r H^*$, EIS curves of $Mg_{1-x}Ce_xNi_{0.9}Al_{0.1}$ ($x=0-0.08$) + 50Ni alloys at 303, 318 and 333 K were measured. 30-h milled $Ce_{0.02}$ and $Ce_{0.04}$ alloys are taken as representatives. Their EIS curves are shown in Fig. 14. By using the data of EIS curves, the Kuriyama diagrams of $\ln(T/R_{ct})$ versus $1/T$ were established according to Eq. (3) and are inset in Fig. 14. From the gradients of the Kuriyama plots, $\Delta_r H^*$ values are allowed to be calculated with no tough. Hence, the functional relationships between $\Delta_r H^*$ values and Ce content as well as milling duration can be acquired, as illustrated in Fig. 15. $\Delta_r H^*$ value of samples firstly descends and soon afterward ascends in the

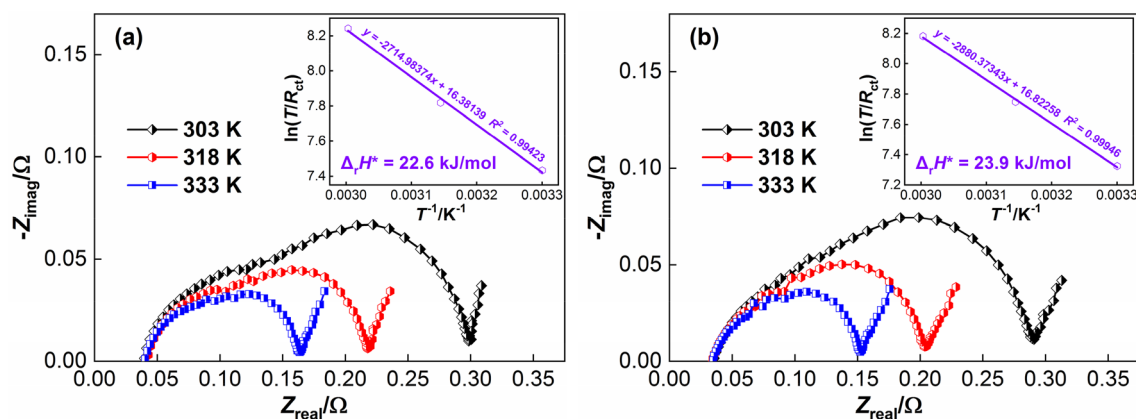


Fig. 14 EIS of as-milled (10 h) $\text{Ce}_{0.02}$ and $\text{Ce}_{0.04}$ alloys at various temperatures. **a** $\text{Ce}_{0.02}$ alloy; **b** $\text{Ce}_{0.04}$ alloy. R^2 Coefficient of determination

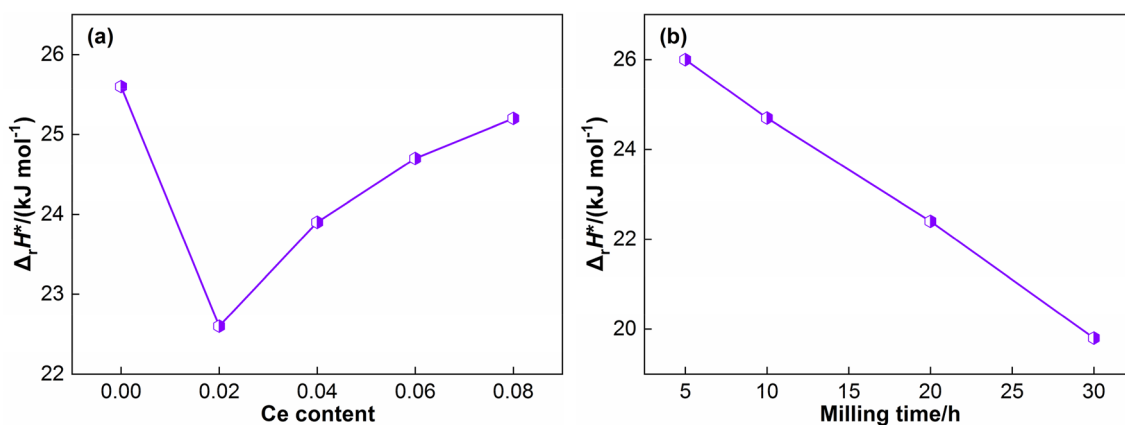


Fig. 15 Evolutions of activation enthalpy $\Delta_r H^*$ values of $\text{Mg}_{1-x}\text{Ce}_x\text{Ni}_{0.9}\text{Al}_{0.1}$ ($x=0-0.08$) + 50Ni alloys with Ce content and milling time. **a** Milled for 10 h; **b** $\text{Ce}_{0.06}$ alloy

wake of Ce content rising, while it keeps declining with the prolonging of milling duration.

The results in Figs. 11, 12 and 15 show that substituting Mg by Ce shows both positive and negative effects on hydrogen diffusion and charge transferring of these alloys, while prolonging milling duration exerts positive influence. The favorable role caused by replacing Mg with Ce is deemed to be contacted with the strengthened corrosion resistance, which is beneficial for suppressing Mg further oxidation inducing a Ni-rich film on sample surface [21] and meanwhile enhancing the electrocatalytic performance of the pole surface. However, too much Ce content brings on an excessively thick CeO_2 passivation layer and hinders the diffusion of hydrogen atoms and charge transfer above the surface of the sample pole. The improved hydrogen diffusing rate and charge transfer velocity by lengthening ball-milling duration are most possibly concerned with Ni coating layer, which has high electrocatalytic activity and promotes hydrogen diffusion and charge transfer. In addition, the main reason for property amelioration by mechanical milling is related to the

added nano-/amorphous microstructure which is beneficial for facilitating the hydrogen diffusing course and the reactivity of charge transferring and leading to a high electrochemical capacity [54]. With the milling duration extending, abundant interfaces and crystal boundaries are generated among the obtained materials, providing convenient channels for hydrogen diffusing and promoting hydrogen absorbing.

4 Conclusions

1. The structural performance of sample alloys shows that the nanocrystalline and amorphous structure can be gotten through milling technology and their grain sizes remarkably shrink with the replacement of Mg by Ce.
2. The as-milled sample alloys exhibit good electrochemical hydrogen absorbing and desorbing property. The cycle stability and discharge capacity of samples are markedly enhanced by ball milling and Ce substitution,

but the discharge capacity presents a maximal value accompanied with Ce content variation.

- The electrochemical kinetics of these samples, containing HRD, I_L , D and charge transfer rate, initially go up and subsequently go down in the wake of adding Ce content, while they grow up clearly with the milling time extension. $\Delta_r H^\circ$ and D values of these samples are considered as the primary controlling elements for their high rate discharge abilities.

Acknowledgements This work was supported by the, 51901105 National Natural Science Foundation of China (Grant Nos. 51761032, 51901105 and 51871125), Natural Science Foundation of Inner Mongolia, China (2019BS05005), and Inner Mongolia University of Science and Technology Innovation Fund (2019QDL-B11).

References

- P. Dibandjo, C. Zlotea, R. Gadiou, C.M. Ghimbeu, F. Cuevas, M. Latroche, E. Leroy, C. Vix-Guterl, *Int. J. Hydrogen Energy* 38 (2013) 952–965.
- L.Z. Ouyang, T.H. Yang, M. Zhu, D. Min, T.Z. Luo, H. Wang, F.M. Xiao, R.H. Tang, *J. Alloy. Compd.* 735 (2018) 98–103.
- X.P. Dong, Y.R. Pang, L.Y. Yang, Q. Wang, Z.Y. Li, *J. Iron Steel Res. Int.* 23 (2016) 459–465.
- A. Eftekhari, B. Fang, *Int. J. Hydrogen Energy* 42 (2017) 25143–25165.
- Y.H. Zhang, Z.C. Jia, Z.M. Yuan, T. Yang, Y. Qi, D.L. Zhao, *J. Iron Steel Res. Int.* 22 (2015) 757–770.
- X. Ding, R.R. Chen, Y.L. Jin, X.Y. Chen, J.J. Guo, Y.Q. Su, H.S. Ding, H.Z. Fu, *J. Power Sources* 374 (2018) 158–165.
- Y.F. Liu, K. Zhong, K. Luo, M.X. Gao, H.G. Pan, Q.D. Wang, *J. Am. Chem. Soc.* 131 (2009) 1862–1870.
- G.H. Ağaoğlu, G. Orhan, *Int. J. Hydrogen Energy* 42 (2017) 8098–8108.
- F. Kong, H. Yan, W. Xiong, Y. Wang, B. Li, J. Li, S. An, *J. Rare Earths* 24 (2006) No. 1, 347–351.
- R.R. Chen, X. Ding, X.Y. Chen, X.Z. Li, Y.Q. Su, J.J. Guo, H.S. Ding, H.Z. Fu, *Int. J. Hydrogen Energy* 44 (2019) 21999–22010.
- Q. Li, K.C. Chou, Q. Lin, L.J. Jiang, F. Zhan, *Int. J. Hydrogen Energy* 29 (2004) 1383–1388.
- Q. Li, Q. Lin, K.C. Chou, L.J. Jiang, *J. Mater. Sci.* 39 (2004) 61–65.
- R.R. Chen, X. Ding, X.Y. Chen, X.Z. Li, J.J. Guo, Y.Q. Su, H.S. Ding, H.Z. Fu, *J. Power Sources* 401 (2018) 186–194.
- Y. Li, Q.F. Gu, Q. Li, T.F. Zhang, *Scripta Mater.* 127 (2017) 102–107.
- Y.P. Pang, Q. Li, *Int. J. Hydrogen Energy* 41 (2016) 18072–18087.
- Q. Li, Y. Li, B. Liu, X.G. Lu, T.F. Zhang, Q.F. Gu, *J. Mater. Chem. A* 5 (2017) 17532–17543.
- D. Feng, H. Sun, Z. Hou, D. Zhao, X. Wang, Y. Zhang, *J. Iron Steel Res. Int.* 24 (2017) 50–58.
- Q. Li, Q. Luo, Q.F. Guo, *J. Mater. Chem. A* 5 (2017) 3848–3864.
- Q. Luo, J.D. Li, B. Li, B. Liu, H.Y. Shao, Q. Li, *J. Magn. Alloy.* 7 (2019) 58–71. <https://doi.org/10.1016/j.jma.2018.12.001>.
- L.J. Huang, Y.X. Wang, J.G. Tang, Y.C. Zhao, G.F. Liu, Y. Wang, J.X. Liu, J.Q. Jiao, W. Wang, B. Jin, L.A. Belfiore, M.J. Kipper, *J. Alloy. Compd.* 694 (2017) 1140–1148.
- Y.H. Zhang, Z.H. Hou, Y. Cai, H.W. Shang, Y. Qi, D.L. Zhao, *J. Iron Steel Res. Int.* 24 (2017) 296–305.
- X.P. Dong, L.Y. Yang, Y.H. Zhang, X.L. Wang, *J. Iron Steel Res. Int.* 16 (2009) No. 3, 83–88.
- M. Balcerzak, M. Nowak, M. Jurczyk, *Int. J. Hydrogen Energy* 42 (2017) 1436–1443.
- Z. Dong, L. Ma, X. Shen, L. Wang, Y. Wu, L. Wang, *Int. J. Hydrogen Energy* 36 (2011) 893–900.
- Y. Wang, X. Wang, C.M. Li, *Int. J. Hydrogen Energy* 35 (2010) 3550–3554.
- S.F. Santos, J.F.R. de Castro, T.T. Ishikawa, E.A. Ticianelli, *J. Mater. Sci.* 43 (2008) 2889–2894.
- H. Sun, D. Feng, Y. Zhang, H. Ren, *Int. J. Hydrogen Energy* 44 (2019) 5382–5388.
- Y. Zhang, W. Zhang, X. Song, P. Zhang, Y. Zhu, Y. Qi, *Trans. Nonferr. Met. Soc. China* 26 (2016) 3219–3231.
- Y.H. Zhang, D.C. Feng, H. Sun, W.G. Bu, Y. Qi, S.H. Guo, *J. Rare Earths* 35 (2017) 280–289.
- K. Young, T. Ouchi, L. Wang, D.F. Wong, *J. Power Sources* 279 (2015) 172–179.
- Y.L. Guo, Y. Li, B. Liu, W.Q. Liu, X. Liang, Q.F. Gu, Q. Li, *J. Alloy. Compd.* 750 (2018) 117–123.
- W. Bu, W. Zhang, J. Gao, Y. Qi, D. Zhao, X. Dong, Y. Zhang, *J. Iron Steel Res. Int.* 26 (2019) 59–68.
- Y. Feng, L. Liu, R. Wang, C. Peng, N. Wang, *Trans. Nonferr. Met. Soc. China* 26 (2016) 1379–1387.
- X.B. Yu, Z.W. Tang, D.L. Sun, L.Z. Ouyang, M. Zhu, *Prog. Mater. Sci.* 88 (2017) 1–48.
- S.H. Hong, M.Y. Song, *Met. Mater. Int.* 22 (2016) 1121–1128.
- L.S. Sun, J. Lin, Z.Y. Cao, F. Liang, L.M. Wang, *J. Alloy. Compd.* 650 (2015) 15–21.
- X.H. Lu, T.Y. Liu, T. Zhai, G.M. Wang, M.H. Yu, S.L. Xie, Y.C. Ling, C.L. Liang, Y.X. Tong, Y. Li, *Adv. Energy Mater.* 4 (2014) 1300994.
- C. Lu, J.X. Zou, X.Q. Zeng, W.J. Ding, *Int. J. Hydrogen Energy* 42 (2017) 15246–15255.
- Y. Pang, Y. Liu, M. Gao, L. Ouyang, J. Liu, H. Wang, M. Zhu, H. Pan, *Nat. Commun.* 5 (2014) 3519.
- X. Zhao, Y. Ding, L. Ma, L. Wang, M. Yang, X. Shen, *Int. J. Hydrogen Energy* 33 (2008) 6727–6733.
- M. Jafarian, O. Azizi, F. Gobal, M.G. Mahjani, *Int. J. Hydrogen Energy* 32 (2007) 1686–1693.
- M.H. Li, Y.F. Zhu, C. Yang, J.G. Zhang, W. Chen, L.Q. Li, *Int. J. Hydrogen Energy* 40 (2015) 13949–13956.
- H.W. Zhang, X.Y. Zheng, T. Wang, X.G. Li, *Intermetallics* 70 (2016) 29–32.
- J. Li, J. Zhou, X. Zhao, M. Yang, L. Ma, X. Shen, *Trans. Nonferr. Met. Soc. China* 25 (2015) 3729–3735. [https://doi.org/10.1016/S1003-6326\(15\)64016-X](https://doi.org/10.1016/S1003-6326(15)64016-X).
- V. Knotek, O. Ekrt, M. Lhotka, D. Vojtěch, *Trans. Nonferr. Met. Soc. China* 26 (2016) 2136–2143.
- B. Liao, Y.Q. Lei, L.X. Chen, G.L. Lu, H.G. Pan, Q.D. Wang, *J. Power Sources* 129 (2004) 358–367.
- V. Yartys, R. Denys, *J. Alloy. Compd.* 645 (2015) S412–S418.
- Y. Zhang, Y. Li, H. Shang, Z. Hou, Y. Qi, D. Zhao, *Trans. Nonferr. Met. Soc. China* 28 (2018) 711–721.
- A.A. Volodin, R.V. Denys, G.A. Tsirlina, B.P. Tarasov, M. Fichtner, V.A. Yartys, *J. Alloy. Compd.* 645 (2015) S288–S291.
- G. Zheng, B.N. Popov, R.E. White, *J. Electrochem. Soc.* 142 (1995) 2695–2698.
- T.T. Zhai, T. Yang, Z.M. Yuan, Y.H. Zhang, *Int. J. Hydrogen Energy* 39 (2014) 14282–14287.
- N. Kuriyama, T. Sakai, H. Miyamura, I. Uehara, H. Ishikawa, T. Iwasaki, *J. Alloy. Compd.* 202 (1993) 183–197.
- H.L. Ding, S.M. Han, Y. Liu, J.S. Hao, Y. Li, J.W. Zhang, *Int. J. Hydrogen Energy* 34 (2009) 9402–9408.
- Y. Liu, H. Pan, M. Gao, Q. Wang, *J. Mater. Chem.* 21 (2011) 4743–4755.